

## Article

# Catalytic Oxidation of Chlorobenzene over Amorphous Manganese-Chromium Catalysts Supported by UiO-66-Derived ZrO<sub>x</sub>

Pengfei Zhu , Qiaosen Yuan, Na Li, Zhaoxia Hu and Shouwen Chen \*

School of Biological and Environmental Engineering, Nanjing University of Science & Technology, Nanjing 210094, China; 317102010045@njjust.edu.cn (P.Z.); yuanqiaosennjust@163.com (Q.Y.); nli@njjust.edu.cn (N.L.); huzhaoxia@njjust.edu.cn (Z.H.)

\* Correspondence: chensw@njjust.edu.cn

**Abstract:** The development of efficient catalysts with longevity to remove chlorobenzene is challenging due to Cl poisoning. Herein, a series of Mn-Cr/ZrO<sub>x</sub> catalysts supported by Zr-based metal-organic framework (UiO-66)-derived ZrO<sub>x</sub> was prepared and investigated for chlorobenzene (CB) catalytic oxidation. MnCr/ZrO<sub>x</sub>-M prepared via a wet impregnation method presented an amorphous structure, indicating the homogeneous dispersion of Cr and Mn, which improved acid and redox properties. 40Mn7Cr3/ZrO<sub>x</sub>-M exhibited the best catalytic activity for chlorobenzene oxidation with T<sub>90</sub> of 293 °C, which is mainly due to the strong interaction between manganese and chromium promoted by the large specific surface area of the ZrO<sub>x</sub> support. Furthermore, 40Mn7Cr3/ZrO<sub>x</sub>-M presented excellent stability for chlorobenzene oxidation.

**Keywords:** catalytic oxidation; chlorobenzene; chromium oxides; synergistic effect



**Citation:** Zhu, P.; Yuan, Q.; Li, N.; Hu, Z.; Chen, S. Catalytic Oxidation of Chlorobenzene over Amorphous Manganese-Chromium Catalysts Supported by UiO-66-Derived ZrO<sub>x</sub>. *Materials* **2024**, *17*, 2103. <https://doi.org/10.3390/ma17092103>

Received: 13 March 2024

Revised: 25 April 2024

Accepted: 25 April 2024

Published: 29 April 2024



**Copyright:** © 2024 by the authors. Licensee MDPI, Basel, Switzerland. This article is an open access article distributed under the terms and conditions of the Creative Commons Attribution (CC BY) license (<https://creativecommons.org/licenses/by/4.0/>).

## 1. Introduction

In recent decades, the emissions of volatile organic compounds (VOCs) have increased dramatically with the rapid development of the industrial economy [1,2]. Among these compounds, chlorinated volatile organic pollutants (CVOCs) are common intermediates and organic solvents in industrial production and waste incineration. Due to their high chemical stability and high toxicity, CVOCs have critically damaged the environment and human health [3,4]. Currently, CVOC treatment technologies include adsorption, photocatalytic degradation, catalytic combustion, ozone oxidation, biological treatment, etc. [5,6]. Catalytic combustion is a very promising technique that can efficiently mineralize CVOCs without producing secondary pollutants [7]. Catalysts play a crucial role in catalytic combustion. A wide range of catalysts are used in this process, including noble metal catalysts, molecular sieve catalysts, and transition metal oxide catalysts [8]. In general, conventional noble metal (e.g., Pt, Pd, and Ru) catalysts exhibit exceptional oxidation capabilities in the destruction of CVOCs. However, their vulnerability to toxic deactivation, sintering, and high prices have strictly limited their practical applications [9–13]. In contrast, transition metal oxide catalysts have attracted high level of concern owing to their resistance to Cl poisoning, low price, and excellent catalytic activity. In addition, the acidity and crystal defects of the transition metal oxides can be customized by doping metal elements, thereby enhancing the selectivity to specific pollutants.

Among non-noble metal catalysts, manganese-based and chromium-based catalysts are very promising owing to their high stability and catalytic oxidation performance [14–16]. Wang et al. successfully prepared Fe-Mn oxide catalysts via the oxalate co-precipitation method [17]. The strong interaction between Fe and Mn increased surface Mn<sup>4+</sup>, which improved their surface acidity and redox performance, thereby promoting the degradation of chlorobenzene. Sun et al. prepared Cr-Ti catalysts, analyzed the combustion of

dichloroethane and chlorobenzene, and revealed that the increase in the specific surface area and Cr<sup>6+</sup> content of the catalyst can improve the catalytic activity [18]. Metal-organic framework materials (MOFs) attracted a high level of concern in adsorption treatment, gas separation, and electrochemistry because of their large specific surface area and varied pore structure [19]. In this paper, porous ZrO<sub>x</sub> derived from a Zr-based metal organic framework (UiO-66) was used as support, providing more active sites and acidic sites, thus enhancing the activity and stability of the catalysts.

Chlorobenzene, a hazardous chemical that can cause irritation, nervous system effects, and potential organ damage, is widely used as an intermediate in chemical production and the petrochemical industry [20–22]. Therefore, it is imperative to develop highly efficient catalysts that exhibit exceptional activity as well as long-term stability for practical applications in the catalytic oxidation of chlorobenzene. In this study, which aimed to develop highly efficient catalysts for chlorobenzene elimination, a series MnCrO<sub>x</sub>/ZrO<sub>x</sub> catalysts were synthesized via a solvothermal method. The crystal structure, surface acidity, redox characteristics, and catalytic combustion performance of the catalysts were studied. We found that the 40Mn7Cr3/ZrO<sub>x</sub>-M presented superior catalytic activity and stability, thereby demonstrating the potential of utilizing ZrO<sub>x</sub> derived from UiO-66 as a promising support for developing high-performance transition metal catalysts.

## 2. Materials and Methods

### 2.1. Chemicals and Materials

Manganese (II) nitrate solution (A.R. grade, Mn(NO<sub>3</sub>)<sub>2</sub>, 50 wt%), Chromium (III) nitrate (A.R. grade, Cr(NO<sub>3</sub>)<sub>3</sub>·9H<sub>2</sub>O), Terephthalic acid (A.R. grade, C<sub>8</sub>H<sub>6</sub>O<sub>4</sub>), and N,N-dimethylformamide (DMF) (A.R. grade, C<sub>3</sub>H<sub>7</sub>NO) were purchased from Aladdin Biochemical Technology Co., Ltd., Shanghai, China. Ethanol (A.R. grade, C<sub>2</sub>H<sub>6</sub>O) was purchased from Nanshi Chemical Reagent Co. Ltd., Nanjing, China. Chlorobenzene (A.R. grade, C<sub>6</sub>H<sub>5</sub>Cl), Zirconium tetrachloride (A.R. grade, ZrCl<sub>4</sub>), and Glacial acetic acid (A.R. grade) were purchased from Merrill Chemical Technology Co. Ltd., Shanghai, China. All chemicals were used without further treatment.

### 2.2. Catalyst Preparation

The Zr-based MOF material UiO-66 was prepared via the solvothermal method [23]. Specifically, 18 mmol (2.99 g) of terephthalic acid and 18 mmol (about 4.19 g) of ZrCl<sub>4</sub> were dissolved in 200 mL N,N-dimethylformamide (DMF), respectively; then, both solutions were mixed together, followed by an addition of 30 mL of glacial acetic acid. After stirring for 30 min, the transparent solution was transferred to a Teflon-lined autoclave, which was then heated at 120 °C for 12 h. The formed solid was centrifuged and then washed 3 times with DMF and absolute ethanol. Finally, the obtained product was dried at 80 °C overnight and denoted as UiO-66. The yield of the UiO-66 was about 80%.

A series of manganese-chromium catalysts was loaded on UiO-66 via the wet impregnation method. Taking 40Mn7Cr3/ZrO<sub>x</sub>-M as an example, the specific preparation steps used were as follows. First, 5 g UiO-66, 0.979 g Cr(NO<sub>3</sub>)<sub>3</sub>·9H<sub>2</sub>O, and 0.375 g 50 wt% Mn(NO<sub>3</sub>)<sub>2</sub> solution were added into 100 mL ultrapure water while stirring. After vigorous stirring at 200 rpm for 0.5 h, the solution was then transferred into a rotary evaporator and evaporated at 80 °C under vacuum. The yield of the loaded MnCr/ZrO<sub>x</sub>-M catalysts was above 90%. The product obtained was dried at 80 °C for 12 h, followed by calcination at 400 °C for 4 h. After grinding, sieving, and tableting (40–60 meshes), a 40Mn7Cr3/ZrO<sub>x</sub>-M catalyst was obtained. ZrO<sub>x</sub>-M was also prepared with the same procedure without the addition of Cr(NO<sub>3</sub>)<sub>3</sub>·9H<sub>2</sub>O and Mn(NO<sub>3</sub>)<sub>2</sub> solutions.

### 2.3. Catalyst Characterization

The catalysts were systematically characterized using various techniques, including X-ray diffraction (XRD), scanning electron microscopy (SEM), energy-dispersive spectroscopy (EDS), N<sub>2</sub> adsorption–desorption analysis, X-ray photoelectron spectroscopy (XPS), H<sub>2</sub>

temperature-programmed reduction (H<sub>2</sub>-TPR), and temperature-programmed desorption of ammonia (NH<sub>3</sub>-TPD).

The samples were analyzed via powder X-ray diffraction technology using a BRUKER D8ADVANCE powder diffractometer. The instrument was equipped with Cu K $\alpha$  radiation ( $\lambda = 1.54178 \text{ \AA}$ ) and operated at 40 kV and 40 mA. The diffraction patterns were recorded within the range of 5 to 90°, employing a scan speed of 10°/min. Scanning electron microscopy (SEM) images were captured using an FEI Quanta 250FEG electron microscope operating at an acceleration voltage ranging from 3 to 15 kV. The elemental distribution of the samples was analyzed through Oxford X-Max energy-dispersive spectroscopy (EDS). The BET surface area ( $S_{\text{BET}}$ ) and pore volume ( $V_{\text{pore}}$ ) of the catalysts were measured at 77 K using a Micromeritics ASAP 2020 automatic specific surface analyzer, followed by pretreatment under vacuum at 200 °C for 2 h. The Brunauer–Emmett–Teller equation was employed to obtain the specific surface area, while the Barrett–Joyner–Halenda (BJH) method was utilized to measure the pore size distribution. The XPS analysis was conducted using a Thermo ESCALAB 250XI spectrometer (Thermo Fisher Scientific, Waltham, MA, USA), which was equipped with AlK radiation (1486.6 eV) as the excitation source.

The H<sub>2</sub>-TPR experiment was conducted using conventional apparatus equipped with a TCD detector. The sample (50 mg) underwent pretreatment at 400 °C for 1 h under a N<sub>2</sub> flow (30 mL/min), followed by cooling to room temperature. Subsequently, the samples were heated in a 5% H<sub>2</sub>/Ar (N<sub>2</sub>) flow (30 mL/min) at a heating rate of 5 °C/min from 50 to 800 °C. To calibrate the amount of H<sub>2</sub> consumption, we utilized complete reduction of a standard CuO sample weighing 50 mg. For NH<sub>3</sub>-TPD analysis, we employed the same apparatus as used for H<sub>2</sub>-TPR. Prior to analysis, each sample (100 mg) was pretreated at 400 °C for an hour with N<sub>2</sub> gas and then cooled down to 50 °C. Next, the samples were exposed to a NH<sub>3</sub> flow (dried gaseous ammonia, 20 mL/min) for at least one hour to achieve saturation of adsorption. Subsequently, the saturated sample was flushed with N<sub>2</sub> gas (30 mL/min) at the same temperature for half an hour in order to eliminate physically adsorbed NH<sub>3</sub>. The desorption process involved heating the samples in N<sub>2</sub> flow (30 mL/min), gradually increasing the temperature from 50 to 800 °C at a rate of 5 °C per minute.

#### 2.4. Catalytic Test

The performance of catalytic combustion for chlorobenzene was evaluated in a fixed-bed reactor consisting of a quartz tube (i.d. = 4 mm) under standard atmospheric pressure. In each experiment, 100 mg of catalysts (40–60 mesh) was immobilized using quartz wool, resulting in a gas hourly space velocity (GHSV) of 20,000 mL·g<sup>-1</sup> h<sup>-1</sup> and a total flow rate of 33.33 mL·min<sup>-1</sup>. The liquid reactant (chlorobenzene) was introduced into the feed stream by passing dried air through a saturator maintained at a temperature of 6 °C. The feed stream was then diluted with dried air generating a feeding flow containing 1000 ppm reactant and 21% O<sub>2</sub>/79% N<sub>2</sub>. Flow rates were regulated using online mass flowmeters. Concentrations of CB and chlorinated byproducts were determined via analysis on an online gas chromatograph (GC3420A, Beifen Ruili Co., Ltd., Beijing, China) equipped with both flame ionization detector (FID) and electron capture detector (ECD) for quantitative assessment of organic compounds. Furthermore, the outlet CO<sub>2</sub> underwent reduction by hydrogen within a methanation furnace before being detected by the same chromatograph system. A K-type thermocouple was inserted into the catalyst to monitor its temperature during the catalytic performance test. Data of catalytic oxidation tests were collected after achieving steady state conditions for at least thirty minutes. The detailed structure of the catalytic test system is shown in Figure 1.

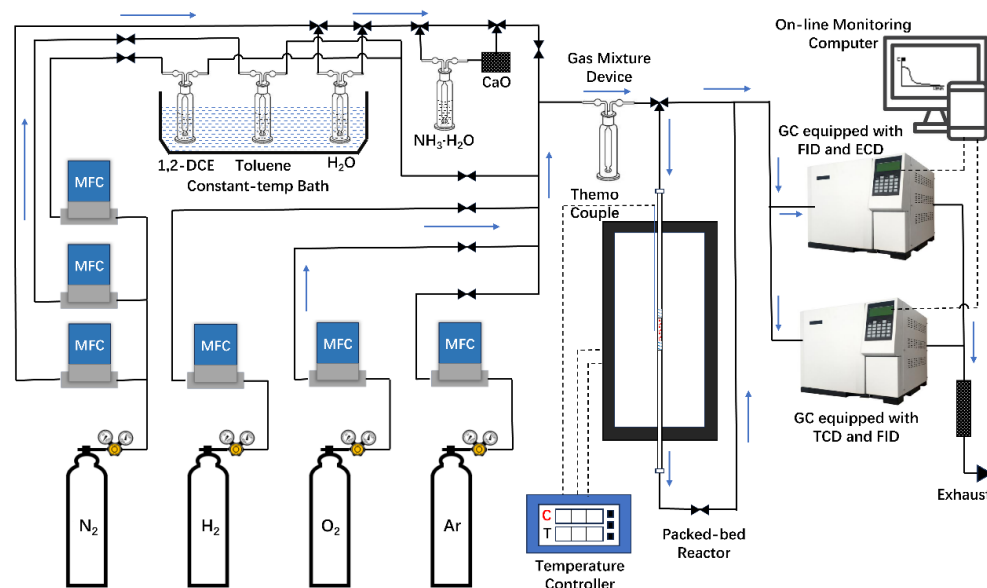


Figure 1. Catalyst performance evaluation system.

The CB conversion rate ( $X_{CB}$ , %),  $CO_2$  yield ( $CO_2yield$ , %) and organic byproduct yield ( $Y_b$ , %) were calculated as follows:

$$X_{CB} = \frac{(CB)_{in} - (CB)_{out}}{(CB)_{in}} \times 100\%, \quad (1)$$

$$CO_2yield = \frac{(CO_2)_{out}}{6 \times (CB)_{in}} \times 100\%, \quad (2)$$

$$Y_b = X_{CB} - CO_2yield, \quad (3)$$

where  $(CB)_{in}$  and  $(CB)_{out}$  are the inlet and outlet concentrations of chlorobenzene, respectively.  $(CO_2)_{out}$  is the outlet concentrations of  $CO_2$ .

The reaction rate of 1,2-dichloroethane was calculated as follows:

$$r = \frac{Q \times X_{CB}}{m} \quad (4)$$

where  $r$  is the reaction rate ( $\text{mol} \cdot \text{g}^{-1} \cdot \text{s}^{-1}$ ),  $Q$  is the molar flow of chlorobenzene ( $\text{mol} \cdot \text{s}^{-1}$ ), and  $m$  is the mass of the catalyst (g).

The stability test for chlorobenzene was performed continuously at 290–320 °C for 100 h under the same conditions as the catalytic combustion test, unless otherwise indicated.

### 3. Results and Discussions

#### 3.1. Catalytic Performance for Chlorobenzene Oxidation

Catalytic oxidation of chlorobenzene was tested on the prepared catalysts, and the light-off curves are shown in Figure 2. The temperatures required for achieving 50% and 90% conversion of chlorobenzene ( $T_{50}$  and  $T_{90}$ ) are listed in Table 1. The sequence in catalytic activity for CB oxidation at  $SV = 20,000 \text{ mL} \cdot \text{g}^{-1} \cdot \text{h}^{-1}$  was  $40\text{Mn}7\text{Cr}3/\text{ZrO}_x\text{-M}$  ( $T_{90} = 293 \text{ }^\circ\text{C}$ ) >  $60\text{Mn}7\text{Cr}3/\text{ZrO}_x\text{-M}$  ( $T_{90} = 295 \text{ }^\circ\text{C}$ ) >  $40\text{Mn}5\text{Cr}5/\text{ZrO}_x\text{-M}$  ( $T_{90} = 296 \text{ }^\circ\text{C}$ ) >  $40\text{Mn}3\text{Cr}7/\text{ZrO}_x\text{-M}$  ( $T_{90} = 301 \text{ }^\circ\text{C}$ ) >  $40\text{Mn}9\text{Cr}1/\text{ZrO}_x\text{-M}$  ( $T_{90} = 311 \text{ }^\circ\text{C}$ ) >  $40\text{Mn}1\text{Cr}9/\text{ZrO}_x\text{-M}$  ( $T_{90} = 315 \text{ }^\circ\text{C}$ ) >  $40\text{CrO}_x/\text{ZrO}_x\text{-M}$  ( $T_{90} = 322 \text{ }^\circ\text{C}$ ) >  $20\text{Mn}7\text{Cr}3/\text{ZrO}_x\text{-M}$  ( $T_{90} = 330 \text{ }^\circ\text{C}$ ) >  $40\text{MnO}_x/\text{ZrO}_x\text{-M}$  ( $T_{90} = 331 \text{ }^\circ\text{C}$ ) >  $\text{ZrO}_x\text{-M}$  ( $T_{90} > 400 \text{ }^\circ\text{C}$ ). Overall, MnCr/ZrO<sub>x</sub>-M catalysts demonstrated excellent performance in the oxidation of chlorobenzene. It is worth noting that the MnCr/ZrO<sub>x</sub>-M catalysts exhibited significantly enhanced activity compared to pristine ZrO<sub>x</sub>-M. The addition of Cr into MnO<sub>x</sub> notably improved the performance of chlorobenzene oxidation, confirming the high activity of Cr-Mn oxides for CB oxidation.

However, excessive Cr doping resulted in a decrease in the amount of acid sites and active oxygen species on the catalyst, leading to reduced catalytic activity. Furthermore, the loading rate of Mn-Cr oxides onto the ZrO<sub>x</sub> substrate played a crucial role in determining the performance of MnCr/ZrO<sub>x</sub>-M. Specifically, 40Mn7Cr3/ZrO<sub>x</sub>-M exhibited the most favorable performance. A loading rate of 20% resulted in a lower proportion of Mn<sup>4+</sup> and Cr<sup>6+</sup>, potentially leading to a decrease in active sites. Conversely, an excessive loading rate of 60% led to a reduction in the specific surface area, indicating a blocked mesoporous structure of ZrO<sub>x</sub>-M. In summary, the Mn/Cr ratio of 7:3 and a loading rate of 40% promote the interaction between Mn, Cr, and ZrO<sub>x</sub> substrates, leading to an augmentation in surface active oxygen and acidic sites of the catalyst. Consequently, this enhances the low-temperature catalytic activity of the catalyst towards chlorobenzene.

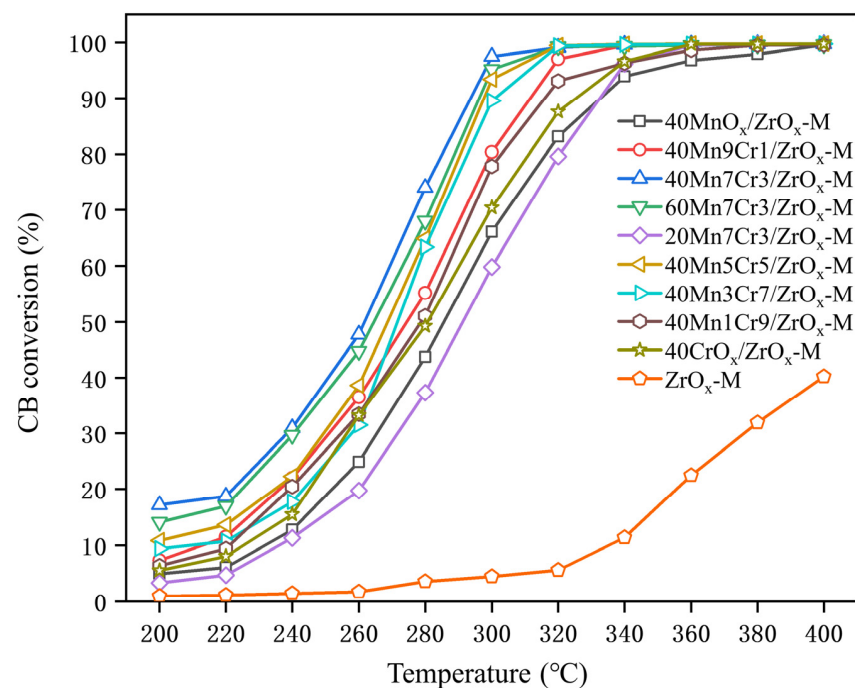


**Figure 2.** The chlorobenzene conversion curves over MnCr/ZrO<sub>x</sub>-M catalysts; gas composition: 1000 ppm chlorobenzene; GHSV = 20,000 h<sup>-1</sup>; catalyst amount: 100 mg.

**Table 1.** Comparison with existing research.

Catalyst	CVOCs	Concentration	Gaseous Hourly Space Velocity	T <sub>90</sub> (°C)	References
MnO <sub>x</sub>	Chlorobenzene	500 ppm	22,500 mL·g <sup>-1</sup> ·h <sup>-1</sup>	301	[24]
Ru/LaMnO <sub>x</sub>	Chlorobenzene	500 ppm	20,000 mL·g <sup>-1</sup> ·h <sup>-1</sup>	356	[25]
Pt-110Mn	Chlorobenzene	1000 ppm	30,000 mL·g <sup>-1</sup> ·h <sup>-1</sup>	290	[26]
La <sub>0.9</sub> Ce <sub>0.1</sub> CoO <sub>3</sub>	Chlorobenzene	1000 ppm	60,000 mL·g <sup>-1</sup> ·h <sup>-1</sup>	422	[27]
40Mn7Cr3/ZrO <sub>x</sub> -M	Chlorobenzene	1000 ppm	20,000 mL·g <sup>-1</sup> ·h <sup>-1</sup>	293	This work

### 3.2. Durability and Stability

In practical applications, catalyst poisoning significantly reduces the operational lifespan of the catalyst and substantially increases the operation cost of the catalytic combustion method [7]. Therefore, the durability and stability of catalysts are equally crucial to their catalytic ability in engineering applications. As depicted in Figure 3A, the catalytic activity remained nearly unchanged after a three-cycle test, indicating excellent durability of the catalyst. Moreover, no significant decline in conversion rates was observed after 100 h of the on-stream test. As depicted in Figure 3B, the conversion of chlorobenzene gradually decreased to 80% at 290 °C within the initial 20 h period. This decline could potentially be

attributed to the accumulation of chlorine species on the surface of catalyst, resulting in the obstruction of active sites. After being heated to 300 °C, the conversion rate exhibited a significant increase and subsequently stabilized at approximately 90%. After reaching a temperature of 320 °C, the accumulated chlorine and carbon species on the catalyst surface desorb, exposing the active sites again. After reaching a temperature of 320 °C, the accumulated chlorine and carbon species were decomposed and the blocked active sites were re-exposed. As a result, the conversion rate was restored and consistently maintained at approximately 99%, with negligible variations observed over a period of 40 h. The ZrO<sub>x</sub> substrate provided a significant number of acidic sites, leading to enhanced stability and a prolonged lifespan. These improvements make the developed catalyst more practical for diverse industrial applications.

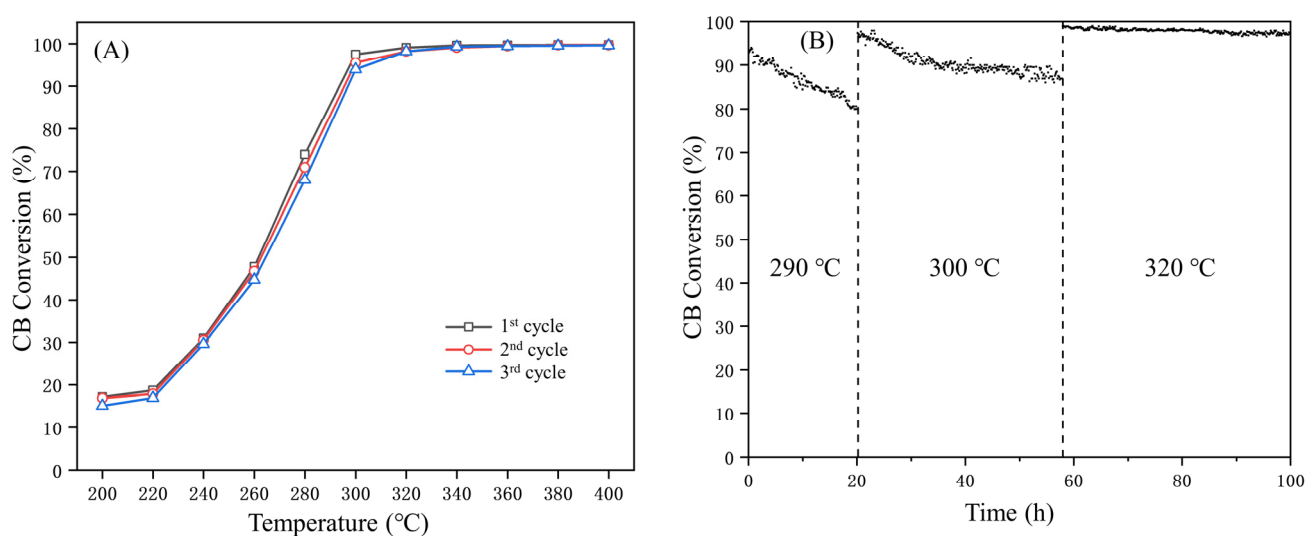


**Figure 3.** The three-cycle conversion curves over 40Mn7Cr3/ZrO<sub>x</sub>-M (A) and the stability of the 40Mn7Cr3/ZrO<sub>x</sub>-M catalyst (B); gas composition: 1000 ppm chlorobenzene; GHSV = 20,000 h<sup>-1</sup>; catalyst amount: 100 mg.

### 3.3. Crystal Structure and Texture Properties

XRD patterns of Mn-Cr/ZrO<sub>x</sub>-M series catalysts and Zr-MOF are shown in Figure 4. The pattern of Zr-MOF (UiO-66) synthesized via the solvothermal method is consistent with the reported literature [28]. After calcination, the typical characteristics peaks of UiO-66 disappeared and obtained ZrO<sub>x</sub>-M catalysts derived from UiO-66 exhibited weak diffraction peaks of orthorhombic phase ZrO<sub>2</sub> (PDF#41-0017), suggesting that UiO-66 decomposed into amorphous ZrO<sub>2</sub>. The EDS results of ZrO<sub>x</sub>-M also proved that organic ligands completely decomposed, leaving only a minimal amount of residual carbon species. Several characteristic peaks at 24.5°, 33.6°, 36.2°, 41.5°, 54.9°, and 65.1° were detected on 40CrO<sub>x</sub>/ZrO<sub>x</sub>-M, and they were assigned to the rhombohedral phase of Cr<sub>2</sub>O<sub>3</sub> (PDF#06-0504) [29]. However, no peaks corresponding to ZrO<sub>2</sub> were detected, suggesting that the Cr species were incorporated into the lattice of ZrO<sub>2</sub> rather than physically loaded onto its surface. This incorporation led to a further decrease in the crystallinity of ZrO<sub>2</sub>. In contrast, diffraction peaks corresponding to both cubic phase Mn<sub>2</sub>O<sub>3</sub> (PDF#10-0069) [30] and ZrO<sub>2</sub> were observed on the 40MnO<sub>x</sub>/ZrO<sub>x</sub>-M, suggesting that MnO<sub>2</sub> was simply loaded on the surface of ZrO<sub>2</sub>. After the introduction of Mn into 40CrO<sub>x</sub>/ZrO<sub>x</sub>-M, the characteristic peaks of Cr<sub>2</sub>O<sub>3</sub> were significantly weakened, indicating that Mn infiltrated the lattice of Cr<sub>2</sub>O<sub>3</sub> and formed an amorphous structure. No diffraction peaks for Mn<sub>5</sub>Cr<sub>5</sub>, Mn<sub>7</sub>Cr<sub>3</sub> and Mn<sub>9</sub>Cr<sub>1</sub> were detected, suggesting that Mn and Cr species were highly dispersed on the ZrO<sub>x</sub> support. The amorphous structure demonstrated strong interactions between manganese and chromium, which promoted the generation of lattice defects and the formation of oxygen vacancies, thus improving catalytic performance [5].

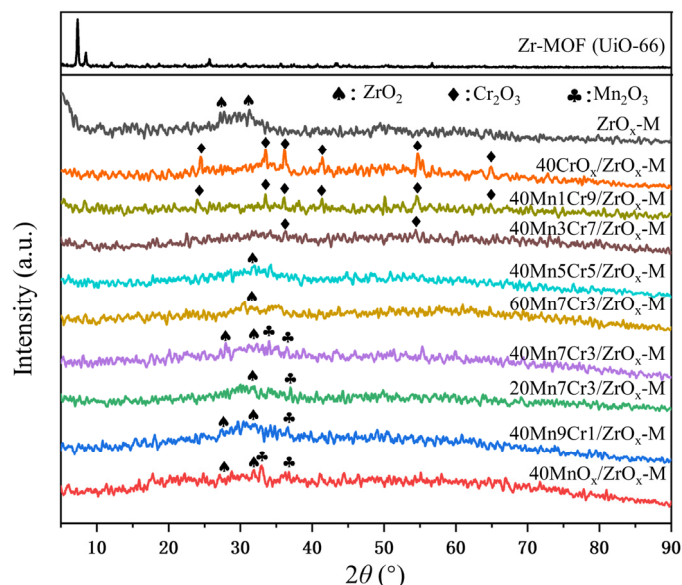


**Figure 4.** XRD patterns of the Mn-Cr/ZrO<sub>x</sub>-M catalysts and Zr-MOF.

The SEM images of Mn-Cr/ZrO<sub>x</sub>-M catalysts are shown in Figure 5. All catalysts presented an irregular clusters structure, resulting in a large specific surface area. This was also confirmed by the N<sub>2</sub> adsorption–desorption results (Figure 6). With the gradual increase in Cr content, the agglomerated particles were transformed into finer particles on the catalyst's surface. However, when the Cr proportion exceeded that of Mn, an accumulation of fine particles occurred on the surface of the ZrO<sub>x</sub>-M support, leading to pore blockage and a significant reduction in specific surface area. This phenomenon is corroborated with the N<sub>2</sub> adsorption–desorption results. Furthermore, it can be observed that the 60Mn7Cr3/ZrO<sub>x</sub>-M catalyst exhibited minimal surface porosity, which could be attributed to excessive loading. After the catalytic stability test, the surface porosity of 40Mn7Cr3/ZrO<sub>x</sub>-M catalyst was slightly decreased, while its fine granular structure remained intact. This result demonstrates the remarkable stability of the prepared catalysts. The utilization of ZrO<sub>2</sub> derived from UiO-66 as a support, in combination with appropriate proportions of Mn and Cr loading, facilitates structural and morphological modifications of catalysts.

To investigate the texture characteristics of the as-prepared catalysts, nitrogen adsorption–desorption measurements were conducted. The isotherms for adsorption–desorption of nitrogen and the distribution of pore sizes (using BJH method) for Mn-Cr/ZrO<sub>x</sub>-M series catalysts are illustrated in Figures 6A and 6B, respectively. The corresponding results, including the specific surface area ( $S_{\text{BET}}$ ), average pore size ( $D_p$ ), and total pore volume ( $V_p$ ) of the catalysts, are summarized in Table 2. All catalysts presented a typical IV adsorption isotherm with H<sub>3</sub>-type hysteresis loops, revealing the mesoporous structure of catalysts, which can be further confirmed by the pore size distribution results [31]. Compared to the conventional sol–gel method and co-precipitation method, catalysts utilizing a porous ZrO<sub>2</sub> substrate exhibited a significantly enhanced specific surface area, thereby facilitating the exposure of acid sites and active sites [32]. The CrO<sub>x</sub> particles exhibited a smaller size compared to MnO<sub>x</sub>, allowing them to infiltrate into the mesoporous channels of MnO<sub>x</sub> and create additional pore structures [33,34]. However, an excessive amount of CrO<sub>x</sub> caused a blockage in the mesopores channel of MnO<sub>x</sub>, leading to a significant decrease in the specific surface area. As the Cr content increased, there was initially an increase in the specific surface area observed for the catalysts, followed by a subsequent reduction. This observation is consistent with the findings from scanning electron microscopy (SEM) analysis. Among all the catalysts, 40Mn7Cr3/ZrO<sub>x</sub>-M exhibited superior specific surface area and pore volume. This resulted in reduced diffusion resistance between chlorobenzene molecules and the active sites of the catalysts, ultimately enhancing their catalytic performance.

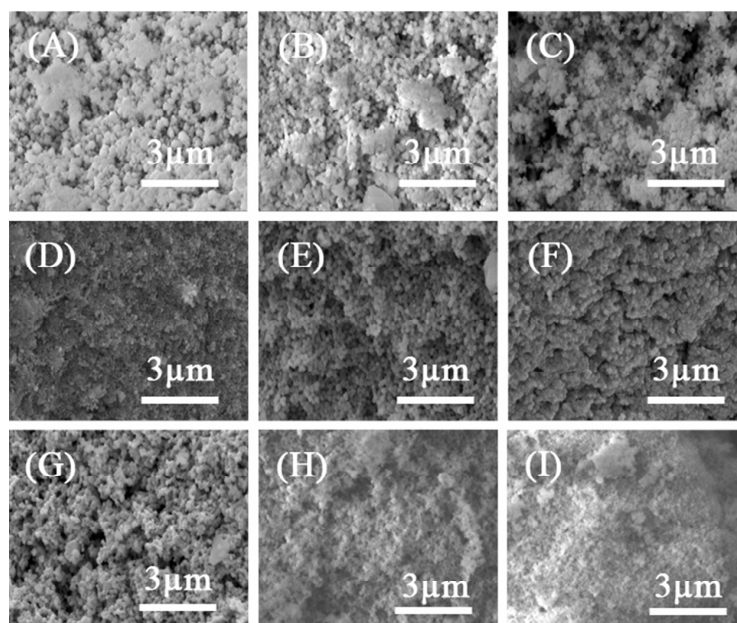


**Figure 5.** SEM images (A–I) of the Mn-Cr/ZrO<sub>x</sub>-M catalysts: (A) 40MnO<sub>x</sub>/ZrO<sub>x</sub>-M; (B) 40Mn9Cr1/ZrO<sub>x</sub>-M; (C) 40Mn7Cr3/ZrO<sub>x</sub>-M; (D) 60Mn7Cr3/ZrO<sub>x</sub>-M; (E) 40Mn5Cr5/ZrO<sub>x</sub>-M; (F) 40Mn3Cr7/ZrO<sub>x</sub>-M; (G) 40Mn1Cr9/ZrO<sub>x</sub>-M; (H) 40CrO<sub>x</sub>/ZrO<sub>x</sub>-M; (I) used 40Mn7Cr3/ZrO<sub>x</sub>-M.

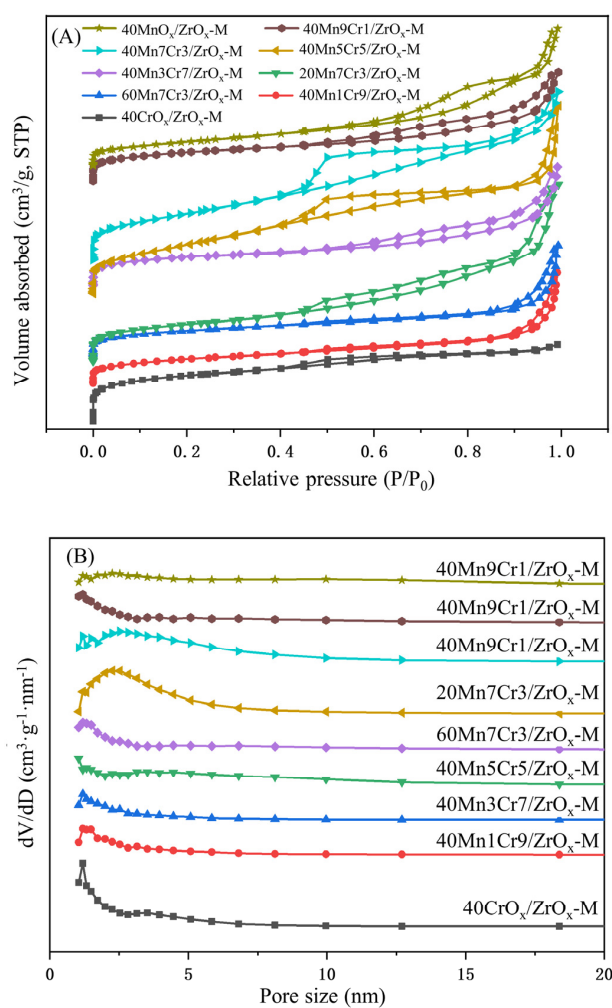


**Figure 6.** N<sub>2</sub> adsorption–desorption isotherms (A) and pore size distribution curves of catalysts (B).

**Table 2.** Characterization results and catalytic performance of the catalysts.

Catalyst	S <sub>BET</sub> (m <sup>2</sup> /g) <sup>a</sup>	D <sub>P</sub> (nm) <sup>b</sup>	V <sub>P</sub> (cm <sup>3</sup> /g) <sup>c</sup>	Mn <sup>4+</sup> /Mn <sup>3+</sup>	Cr <sup>6+</sup> /Cr <sup>3+</sup>	O <sub>ads</sub> /O <sub>latt</sub>	T <sub>50</sub> (°C)	T <sub>90</sub> (°C)
40MnO <sub>x</sub> /ZrO <sub>x</sub> -M	113.1	9.7	0.27	-	-	-	285	331
40Mn9Cr1/ZrO <sub>x</sub> -M	136.6	6.3	0.22	1.53	0.43	0.56	274	311
40Mn7Cr3/ZrO <sub>x</sub> -M	231.4	5.8	0.34	1.68	0.50	0.79	262	293
20Mn7Cr3/ZrO <sub>x</sub> -M	238.9	5.9	0.35	-	-	-	290	330
60Mn7Cr3/ZrO <sub>x</sub> -M	140.5	6.5	0.23	-	-	-	264	295
40Mn5Cr5/ZrO <sub>x</sub> -M	172.0	8.3	0.34	1.78	0.71	0.59	269	296
40Mn3Cr7/ZrO <sub>x</sub> -M	110.9	7.4	0.20	-	-	-	271	301
40Mn1Cr9/ZrO <sub>x</sub> -M	121.5	7.0	0.21	-	-	-	279	315
40CrO <sub>x</sub> /ZrO <sub>x</sub> -M	218.4	2.9	0.16	-	-	-	280	322
ZrO <sub>x</sub> -M	-	-	-	-	-	-	>400	>400

<sup>a</sup> BET specific surface area. <sup>b</sup> Total pore volume estimated at  $p/p_0 = 0.99$ . <sup>c</sup> BJH pore diameter calculated from the absorption branch.

### 3.4. Chemical States, Redox, and Acidity Properties

The acidic sites of the catalysts were studied via NH<sub>3</sub>-TPD, and the corresponding results are presented in Figure 7. It has been proven that NH<sub>3</sub> desorption temperature reflects the acidity of a catalyst's surface and that the desorption peak area reveals the quantity of acid sites [35]. NH<sub>3</sub> desorption curves of the catalysts presented a wide ammonia desorption peak, which could be divided into weak acidic site peaks (50–200 °C) and strong acidic site peaks (200–400 °C) [36,37]. Recent studies have demonstrated that the presence of weak acid sites enhances the adsorption of chlorobenzene, while strong acid sites promote the desorption of chlorine intermediates [38–40]. Both types of acid sites contribute to increased catalytic performance. Figure 7 demonstrates the substantial occurrence of weak acid sites in all Mn-Cr/ZrO<sub>x</sub>-M catalysts. The desorption peaks observed at temperatures ranging from 50 to 200 °C primarily originated from the ZrO<sub>x</sub>-M support, which was closely related to the high specific surface area of the catalysts [41]. The addition of Cr significantly increased the amount of weak acid sites in Mn1Cr9 to the Mn7Cr3 samples, which promoted the catalytic oxidation of chlorobenzene [42]. The strong interaction between well-dispersed Mn and Cr on the catalyst surface promoted the formation of surface hydroxyl groups, thereby forming strong acid sites corresponding to the broad peak above 200 °C [26]. Cr notably increased the high-temperature peak area of the profiles, suggesting that the catalysts had abundant strong acid sites, which promoted the deep oxidation of CVOCs. The moderate doping of Cr leads to a shift in the NH<sub>3</sub> desorption peak towards higher temperatures, thereby increasing the acidity of the catalysts. This enhancement promotes the deep oxidation of CVOCs. However, an excessive doping rate of Cr may weaken the interaction between Mn and Cr, leading to a significant reduction in the number of strong acid sites and consequently reducing catalytic performance.

The redox property of Mn-Cr/ZrO<sub>x</sub>-M series catalysts was investigated via H<sub>2</sub>-TPR, and their profiles are shown in Figure 8. In general, the valence state and the quantity of active oxygen are crucial to redox performance [43]. For ZrO<sub>x</sub>-M, a weaker reduction peak was observed at around 520 °C, suggesting that the pristine ZrO<sub>x</sub>-M support exhibited relatively modest reducing performance. The profile of 40MnO<sub>x</sub>/ZrO<sub>x</sub> displayed two reduction peaks at 375 °C and 440 °C, corresponding to a reduction in Mn<sup>4+</sup> and Mn<sup>3+</sup>, respectively [44]. Generally speaking, the reduction in MnO<sub>x</sub>-based catalysts, which undergo successive processes of MnO<sub>2</sub> → Mn<sub>3</sub>O<sub>4</sub>/Mn<sub>2</sub>O<sub>3</sub> → MnO, corresponds to low-temperature reduction peaks (<400 °C) and high-temperature reduction peaks, respectively [45]. The 40CrO<sub>x</sub>/ZrO<sub>x</sub>-M catalyst presented a significant reduction peak at 300 °C, corresponding to the reduction in Cr<sup>6+</sup> to Cr<sup>3+</sup> [46]. After doping Cr into 40MnO<sub>x</sub>/ZrO<sub>x</sub>-M, it was observed that the reduction peaks of Mn<sup>4+</sup> and Cr<sup>6+</sup> merged to form a larger peak. This suggests that there was a strong interaction between MnO<sub>x</sub> and CrO<sub>x</sub>, which enhanced the mobility of the surface lattice oxygen and subsequently improved catalytic activity [47]. Moreover, the addition of Cr led to increased reduction peak areas that shifted towards lower temperatures, thereby enhancing the redox performance at low temperatures [26]. However,

excessive Cr doping resulted in the absence of a reduction peak at 375 °C, indicating the weaker redox ability of Mn<sub>3</sub>Cr<sub>7</sub> and Mn<sub>1</sub>Cr<sub>9</sub>. The 40Mn<sub>7</sub>Cr<sub>3</sub>/ZrO<sub>x</sub>-M catalyst exhibited the largest H<sub>2</sub> reduction peak at the lowest temperature, suggesting excellent redox activity. These findings are consistent with the results of the catalytic performance test.

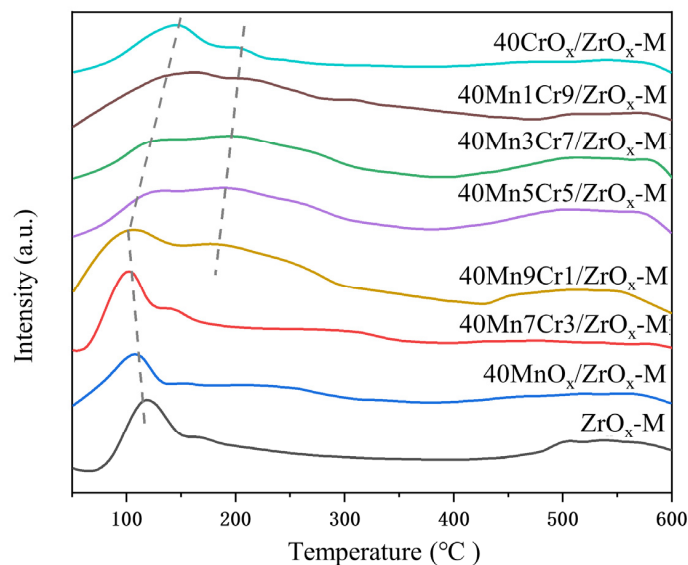


**Figure 7.** NH<sub>3</sub>-TPD profiles of the Mn-Cr/ZrO<sub>x</sub>-M catalysts.

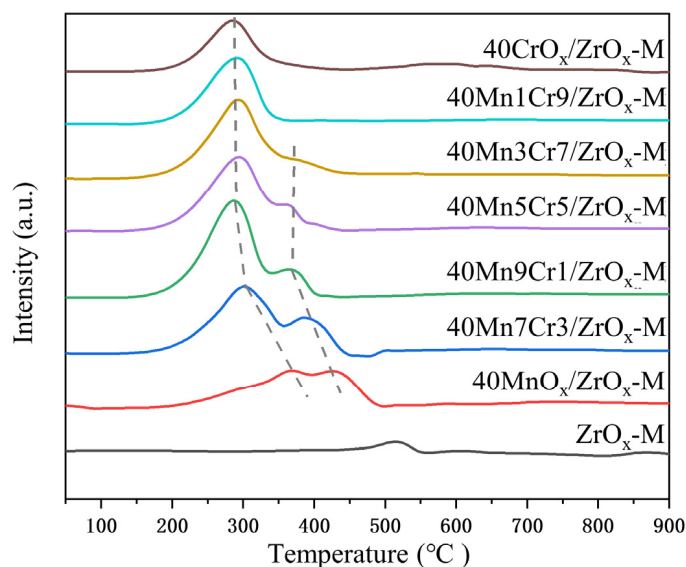


**Figure 8.** H<sub>2</sub>-TPR profiles of the Mn-Cr/ZrO<sub>x</sub>-M catalysts.

Chemical states and oxidation states of the catalysts were studied via Mn 2p, Cr 2p, and Zr 3d XPS spectra, the patterns of which are shown in Figure 9, and the quantitative results are summarized in Table 1. The Mn 2p spectra (Figure 9A) exhibited two binding energy peaks in the range of 642.9–643.2 eV and 641.4–641.9 eV regions, which were attributed to Mn<sup>4+</sup> and Mn<sup>3+</sup>, respectively. This demonstrates the coexistence of Mn<sup>4+</sup> and Mn<sup>3+</sup> on the catalyst's surface. However, Mn<sup>4+</sup> characteristic peaks were absent in the XRD patterns, indicating that Mn<sup>4+</sup> species were uniformly dispersed on the surface of the catalyst with an amorphous structure. With the addition of Cr, the Mn 2P spectra shifted towards higher-binding-energy regions, indicating an increased electron cloud density in Mn<sup>4+</sup> and Mn<sup>3+</sup> due to the interaction between Cr and Mn [48]. In addition, the peak position of Zr also shifted to higher-binding-energy regions with the doping of Cr, which

revealed a strong interaction between the  $\text{ZrO}_x$  support and Mn-Cr oxides. According to the results presented in Table 2, the proportion of  $\text{Mn}^{4+}$  noticeably increased following Cr doping due to the strong interaction between the two elements. Moreover, higher-valence Mn species are more favorable for promoting oxidation reactions and facilitating the generation of oxygen vacancies [49]. For the Cr 2p spectrum, the binding energy peaks at 588.4–588.8 eV and 579.4–579.6 eV regions were assigned to  $\text{Cr}^{6+}$ , and the binding energy peaks at 586.6–586.7 eV and 576.9–577.0 eV regions were attributed to  $\text{Cr}^{3+}$ . These results suggest that  $\text{Cr}^{6+}$  and  $\text{Cr}^{3+}$  coexist on the catalyst's surface. The absence of characteristic peaks for  $\text{CrO}_x$  in XRD patterns indicates that  $\text{Cr}^{6+}$  is uniformly dispersed on the catalyst's amorphous surface structure, which enhances the deep oxidation of chlorobenzene [18]. Broad and asymmetric peaks were observed in the O 1s spectra. The peak at an electronic binding energy of 531.6–531.8 eV was assigned to adsorbed oxygen ( $\text{O}_{\text{ads}}$ ), while the peak at 530.1–530.4 eV was attributed to lattice oxygen ( $\text{O}_{\text{latt}}$ ). Previous studies have demonstrated that  $\text{O}_{\text{ads}}$  is the most active oxygen species, promoting the transportation and transformation of oxygen species [50–52]. Therefore, a higher content of  $\text{O}_{\text{ads}}$  improves catalytic combustion performance. According to the peak area results in Table 1, it can be seen that the 40Mn7Cr3/ $\text{ZrO}_x$ -M exhibited the largest ratio of  $\text{O}_{\text{ads}}/\text{O}_{\text{latt}}$ , which was consistent with the catalytic performance results.

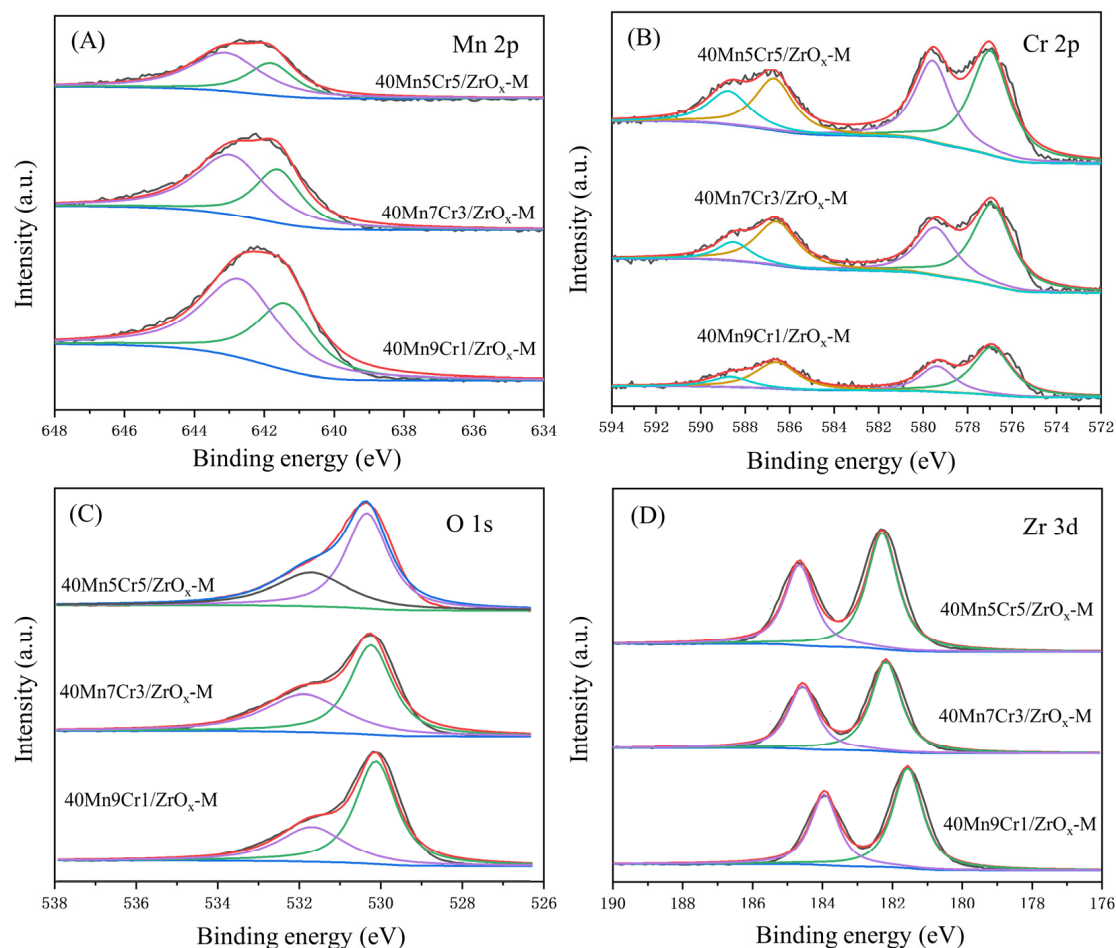


**Figure 9.** XPS spectra of the MnCr/ $\text{ZrO}_x$ -M catalysts: (A) Mn 2p; (B) Cr 2p; (C) O 1s; (D) Zr 3d.

As shown in Figure 10, the EPR profile of the Mn-Cr/ $\text{ZrO}_x$ -M catalysts presented a signal-centered  $g = 2.003$ , which could be attributed to the electrons trapped in oxygen vacancies [51]. In addition, the EPR signal intensity of 40Mn7Cr3/ $\text{ZrO}_x$ -M was significantly higher than that of  $\text{ZrO}_x$ -M. This suggests that the loaded  $\text{MnCrO}_x$  can offer abundant oxygen vacancies.

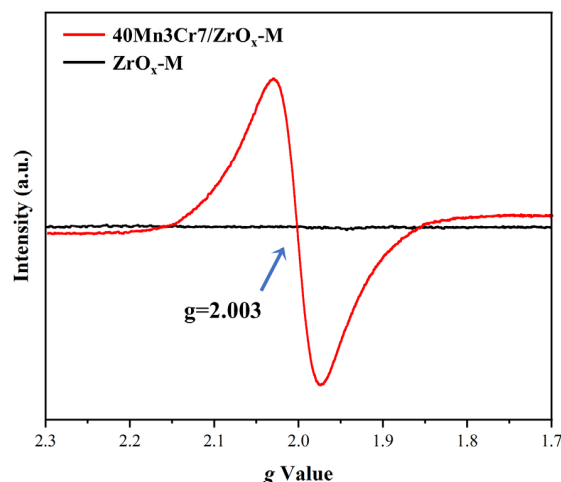


Figure 10. EPR profiles of the Mn-Cr/ZrO<sub>x</sub>-M catalysts.

#### 4. Conclusions

In this study, a series of Mn-Cr/ZrO<sub>x</sub>-M catalysts with different proportions of manganese-chromium oxides were synthesized using ZrO<sub>x</sub> derived from UiO-66 as a substrate. After the loading of the Mn-Cr oxide, the catalytic performance of the MnCr/ZrO<sub>x</sub>-M catalyst was significantly enhanced compared to that of pristine ZrO<sub>x</sub>-M. Among the MnCr/ZrO<sub>x</sub>-M catalysts, the 40Mn7Cr3/ZrO<sub>x</sub>-M with mesoporous-structured irregular clusters achieved superior activity with the T<sub>90</sub> of 293 °C for the catalytic oxidation of chlorobenzene at the WHSV of 20,000 h<sup>-1</sup>. Furthermore, the 40Mn7Cr3/ZrO<sub>x</sub>-M catalyst exhibited developed catalytic activity and durability, making it a promising candidate for practical applications. This exceptional catalytic performance can be mainly attributed to its remarkable oxidizing capability and the abundant presence of active oxygen species on its surface. These characteristics are a direct consequence of the strong interaction between Mn and Cr, resulting in the formation of amorphous MnCrO<sub>x</sub> oxides. Moreover, the mesoporous structure of the ZrO<sub>x</sub>-M substrate promotes the exposure of acid sites and active sites, thereby enhancing both the low-temperatures catalytic performance and lifespan of the catalyst. In summary, this study provides valuable insights into the effective application of additional components to enhance the production of reactive oxygen species for the purpose of CVOCs' catalytic decomposition.

**Author Contributions:** Conceptualization, P.Z. and S.C.; methodology, P.Z.; validation, N.L., Z.H. and S.C.; formal analysis, P.Z. and Q.Y.; investigation, P.Z.; data curation, P.Z.; writing—original draft preparation, P.Z.; writing—review and editing, Z.H. and S.C.; project administration, S.C.; funding acquisition, S.C. All authors have read and agreed to the published version of the manuscript.

**Funding:** This research was funded by Fundamental Research Funds for the Central Universities (30920021114), China.

**Institutional Review Board Statement:** Not applicable.

**Informed Consent Statement:** Not applicable.

**Data Availability Statement:** Data will be made available on request.

**Conflicts of Interest:** The authors declare no conflict of interest.

#### References

- Li, N.; Gaillard, F. Catalytic combustion of toluene over electrochemically promoted Ag catalyst. *Appl. Catal. B Environ.* **2009**, *88*, 152–159. [[CrossRef](#)]
- Pan, C.; Wang, W.; Zhang, Y.; Nam, J.C.; Wu, F.; You, Z.; Xu, J.; Li, J. Porous graphitized carbon-supported FeOCl as a bifunctional adsorbent-catalyst for the wet peroxide oxidation of chlorinated volatile organic compounds: Effect of mesopores and mechanistic study. *Appl. Catal. B Environ.* **2023**, *330*, 122659. [[CrossRef](#)]

3. Huang, B.; Lei, C.; Wei, C.; Zeng, G. Chlorinated volatile organic compounds (Cl-VOCs) in environment—Sources, potential human health impacts, and current remediation technologies. *Environ. Int.* **2014**, *71*, 118–138. [[CrossRef](#)] [[PubMed](#)]
4. Zhao, X.; Xu, D.; Wang, Y.; Zheng, Z.; Li, K.; Zhang, Y.; Zhan, R.; Lin, H. Electric field assisted benzene oxidation over Pt-Ce-Zr nano-catalysts at low temperature. *J. Hazard. Mater.* **2021**, *407*, 124349. [[CrossRef](#)] [[PubMed](#)]
5. Lee, J.E.; Ok, Y.S.; Tsang, D.C.W.; Song, J.; Jung, S.C.; Park, Y.K. Recent advances in volatile organic compounds abatement by catalysis and catalytic hybrid processes: A critical review. *Sci. Total Environ.* **2020**, *719*, 137405. [[CrossRef](#)] [[PubMed](#)]
6. Mustafa, M.F.; Liu, Y.; Duan, Z.; Guo, H.; Xu, S.; Wang, H.; Lu, W. Volatile compounds emission and health risk assessment during composting of organic fraction of municipal solid waste. *J. Hazard. Mater.* **2017**, *327*, 35–43. [[CrossRef](#)] [[PubMed](#)]
7. Lin, F.; Zhang, Z.; Li, N.; Yan, B.; He, C.; Hao, Z.; Chen, G. How to achieve complete elimination of Cl-VOCs: A critical review on byproducts formation and inhibition strategies during catalytic oxidation. *Chem. Eng. J.* **2021**, *404*, 126534. [[CrossRef](#)]
8. Hou, Z.; Pei, W.; Zhang, X.; Zhang, K.; Liu, Y.; Deng, J.; Jing, L.; Dai, H. Rare earth oxides and their supported noble metals in application of environmental catalysis. *J. Rare Earths* **2020**, *38*, 819–839. [[CrossRef](#)]
9. Huang, J.; Zhang, Y.; Hao, Z.; Zhang, Y. Preparation of rare earth metal ions promoted MnOx@halloysite catalyst for highly efficient catalytic oxidation of toluene. *Appl. Clay Sci.* **2023**, *244*, 107081. [[CrossRef](#)]
10. Shi, Y.; Wang, J.; Zhou, R. Pt-support interaction and nanoparticle size effect in Pt/CeO<sub>2</sub>-TiO<sub>2</sub> catalysts for low temperature VOCs removal. *Chemosphere* **2021**, *265*, 129127. [[CrossRef](#)]
11. Topka, P.; Delaigle, R.; Kaluža, L.; Gaigneaux, E.M. Performance of platinum and gold catalysts supported on ceria–zirconia mixed oxide in the oxidation of chlorobenzene. *Catal. Today* **2015**, *253*, 172–177. [[CrossRef](#)]
12. Guo, Y.; Gao, Y.; Li, X.; Zhuang, G.; Wang, K.; Zheng, Y.; Sun, D.; Huang, J.; Li, Q. Catalytic benzene oxidation by biogenic Pd nanoparticles over 3D-ordered mesoporous CeO<sub>2</sub>. *Chem. Eng. J.* **2019**, *362*, 41–52. [[CrossRef](#)]
13. Chen, Z.; Mao, J.; Zhou, R. Preparation of size-controlled Pt supported on Al<sub>2</sub>O<sub>3</sub> nanocatalysts for deep catalytic oxidation of benzene at lower temperature. *Appl. Surf. Sci.* **2019**, *465*, 15–22. [[CrossRef](#)]
14. Zhou, Z.; Li, Q.; Su, G.; Pang, J.; Sun, B.; Meng, J.; Shi, B. Catalytic degradation of chlorinated volatile organic compounds (CVOCs) over Ce-Mn-Ti composite oxide catalysts. *J. Environ. Sci.* **2024**, *138*, 326–338. [[CrossRef](#)] [[PubMed](#)]
15. Zhang, J.; Zhang, L.; Cheng, Y.; Liu, Y. Construction of oxygen vacancies in δ-MnO<sub>2</sub> for promoting low-temperature toluene oxidation. *Fuel* **2023**, *332*, 126104. [[CrossRef](#)]
16. Ye, N.; Zheng, J.; Xie, K.; Jiang, B.; Zuo, S. Performance of mesoporous CeO<sub>2</sub>-Cr<sub>2</sub>O<sub>3</sub> mixed metal oxides applied to benzene catalytic combustion. *J. Rare Earths* **2023**, *41*, 889–895. [[CrossRef](#)]
17. Wang, Y.; Wang, G.; Deng, W.; Han, J.; Qin, L.; Zhao, B.; Guo, L.; Xing, F. Study on the structure-activity relationship of Fe-Mn oxide catalysts for chlorobenzene catalytic combustion. *Chem. Eng. J.* **2020**, *395*, 125172. [[CrossRef](#)]
18. Sun, W.; Gong, B.; Pan, J.; Wang, Y.; Xia, H.; Zhang, H.; Dai, Q.; Wang, L.; Wang, X. Catalytic combustion of CVOCs over Cr Ti-oxide catalysts. *J. Catal.* **2020**, *391*, 132–144. [[CrossRef](#)]
19. Ryu, U.; Jee, S.; Rao, P.C.; Shin, J.; Ko, C.; Yoon, M.; Park, K.S.; Choi, K.M. Recent advances in process engineering and upcoming applications of metal-organic frameworks. *Coord. Chem. Rev.* **2021**, *426*, 213544. [[CrossRef](#)]
20. Meng, J.; Fu, Y.; Chen, S.; Zhang, H.; Li, Z.; Wang, X.; Luo, J.; Zhou, Y.; Luo, S.; Qin, H. Hollow zeolite-based V-Cu bimetallic oxide catalyst for remarkable catalytic oxidation of chlorobenzene. *Sep. Purif. Technol.* **2023**, *326*, 124775. [[CrossRef](#)]
21. Wan, J.; Tao, F.; Shi, Y.; Shi, Z.; Liu, Y.; Wu, G.; Kan, J.; Zhou, R. Designed preparation of nano rod shaped CeO<sub>2</sub>-MnO catalysts with different Ce/Mn ratios and its highly efficient catalytic performance for chlorobenzene complete oxidation: New insights into structure–activity correlations. *Chem. Eng. J.* **2022**, *433*, 133788. [[CrossRef](#)]
22. Liu, J.; Zuo, S.; Lin, S.; Shan, B.; Zhou, X.; Zhao, J.; Qi, C.; Yang, P. Promoting the performance of Nb<sub>2</sub>O<sub>5</sub> by doping transition metal oxide for catalytic degradation of monochlorobenzene and toluene. *J. Mater. Res. Technol.* **2023**, *25*, 3642–3653. [[CrossRef](#)]
23. Yang, T.; Gao, Y.; He, Q.; Chai, Y.; Qin, P.; Wu, Z.; Liu, C.; Gong, X.; Liang, Y. Preparation and application of UiO-66(Zr) and its derivatives as catalysts in lignocellulosic biomass conversion. *Chem. Eng. J.* **2024**, *486*, 149971. [[CrossRef](#)]
24. Duan, X.; Zhao, T.; Yang, Z.; Niu, B.; Li, G.; Li, B.; Zhang, Z.; Cheng, J.; Hao, Z. Oxygen activation-boosted manganese oxide with unique interface for chlorobenzene oxidation: Unveiling the roles and dynamic variation of active oxygen species in heterogeneous catalytic oxidation process. *Appl. Catal. B Environ.* **2023**, *331*, 122719. [[CrossRef](#)]
25. Duan, X.; Zhao, T.; Niu, B.; Wei, Z.; Li, G.; Zhang, Z.; Cheng, J.; Hao, Z. Simultaneously Constructing Active Sites and Regulating Mn-O Strength of Ru-Substituted Perovskite for Efficient Oxidation and Hydrolysis Oxidation of Chlorobenzene. *Adv. Sci.* **2023**, *10*, e2205054. [[CrossRef](#)] [[PubMed](#)]
26. Chen, G.; Cai, Y.; Zhang, H.; Hong, D.; Shao, S.; Tu, C.; Chen, Y.; Wang, F.; Chen, B.; Bai, Y.; et al. Pt and Mo Co-Decorated MnO<sub>2</sub> Nanorods with Superior Resistance to H<sub>2</sub>O, Sintering, and HCl for Catalytic Oxidation of Chlorobenzene. *Environ. Sci. Technol.* **2021**, *55*, 14204–14214. [[CrossRef](#)] [[PubMed](#)]
27. Pérez, H.A.; López, C.A.; Cadús, L.E.; Agüero, F.N. Catalytic feasibility of Ce-doped LaCoO<sub>3</sub> systems for chlorobenzene oxidation: An analysis of synthesis method. *J. Rare Earths* **2022**, *40*, 897–905. [[CrossRef](#)]
28. Hu, P.; Liang, X.; Yaseen, M.; Sun, X.; Tong, Z.; Zhao, Z.; Zhao, Z. Preparation of highly-hydrophobic novel N-coordinated UiO-66(Zr) with dopamine via fast mechano-chemical method for (CHO-/Cl)-VOCs competitive adsorption in humid environment. *Chem. Eng. J.* **2018**, *332*, 608–618. [[CrossRef](#)]

29. Zhang, X.; Liu, Y.; Deng, J.; Zhao, X.; Zhang, K.; Yang, J.; Han, Z.; Jiang, X.; Dai, H. Three-dimensionally ordered macroporous Cr<sub>2</sub>O<sub>3</sub>–CeO<sub>2</sub>: High-performance catalysts for the oxidative removal of trichloroethylene. *Catal. Today* **2020**, *339*, 200–209. [[CrossRef](#)]
30. Lin, F.; Zhang, Z.; Xiang, L.; Zhang, L.; Cheng, Z.; Wang, Z.; Yan, B.; Chen, G. Efficient degradation of multiple Cl-VOCs by catalytic ozonation over MnO catalysts with different supports. *Chem. Eng. J.* **2022**, *435*, 134807. [[CrossRef](#)]
31. Wang, X.; Wang, C.; Liu, Y.; Zhang, X.; Yang, H.; Chen, Y.; Chen, H. Modification of a micro-mesoporous Ni/ZSM-5 catalyst for steam reforming of toluene. *Powder Technol.* **2023**, *429*, 118933. [[CrossRef](#)]
32. Zhou, Z.; Liu, L.; Liu, X.; Zhou, Y.; Li, C.; Peng, D.; Xu, J.; Wang, C.; Cao, X.E. Direct combustion of wet/dry solution-impregnated cigarette butts for nano-FeOx synthesis: Effects of combustion conditions and NO reduction ability. *Colloid. Interface Sci. Commun.* **2022**, *46*, 100562. [[CrossRef](#)]
33. Hosseini, S.A.; Niaei, A.; Salari, D.; Alvarez-Galvan, M.C.; Fierro, J.L.G. Study of correlation between activity and structural properties of Cu-(Cr, Mn and Co)<sub>2</sub> nano mixed oxides in VOC combustion. *Ceram. Int.* **2014**, *40*, 6157–6163. [[CrossRef](#)]
34. González-Cobos, J.; Mylonoyannis, B.; Chai, G.; Zhang, W.; Tian, C.; Kaddouri, A.; Gil, S. Low-temperature gas-phase toluene catalytic combustion over modified CoCr<sub>2</sub>O<sub>4</sub> spinel catalysts: Effect of Co/Cr content and calcination temperature. *Appl. Catal. A Gen.* **2023**, *657*, 119162. [[CrossRef](#)]
35. Gao, N.; Zhou, Y.; Fan, M.; Xu, H.; Chen, Y.; Shen, S. Promoting effect and role of alkaline earth metal added to ZrO<sub>2</sub>-TiO<sub>2</sub>-supported CeO<sub>2</sub> for dichloromethane oxidation. *Chem. Eng. J.* **2020**, *396*, 125193. [[CrossRef](#)]
36. Zhang, N.; Guo, Y.; Guo, Y.; Dai, Q.; Wang, L.; Dai, S.; Zhan, W. Synchronously constructing the optimal redox-acidity of sulfate and RuOx Co-modified CeO<sub>2</sub> for catalytic combustion of chlorinated VOCs. *Chem. Eng. J.* **2023**, *454*, 140391. [[CrossRef](#)]
37. Wan, J.; Yang, P.; Guo, X.; Zhou, R. Elimination of 1,2-dichloroethane over (Ce, Cr) O<sub>2</sub>/Nb<sub>2</sub>O<sub>5</sub> catalysts: Synergistic performance between oxidizing ability and acidity. *Chin. J. Catal.* **2019**, *40*, 1100–1108. [[CrossRef](#)]
38. Yang, P.; Fan, S.; Chen, Z.; Bao, G.; Zuo, S.; Qi, C. Synthesis of Nb<sub>2</sub>O<sub>5</sub> based solid superacid materials for catalytic combustion of chlorinated VOCs. *Appl. Catal. B Environ.* **2018**, *239*, 114–124. [[CrossRef](#)]
39. Huang, Q.; Xue, X.; Zhou, R. Decomposition of 1,2-dichloroethane over CeO<sub>2</sub> modified USY zeolite catalysts: Effect of acidity and redox property on the catalytic behavior. *J. Hazard. Mater.* **2010**, *183*, 694–700. [[CrossRef](#)]
40. Chen, G.; Hong, D.; Xia, H.; Sun, W.; Shao, S.; Gong, B.; Wang, S.; Wu, J.; Wang, X.; Dai, Q. Amorphous and homogeneously Zr-doped MnOx with enhanced acid and redox properties for catalytic oxidation of 1,2-Dichloroethane. *Chem. Eng. J.* **2022**, *428*, 131067. [[CrossRef](#)]
41. Chai, S.; Li, S.; Li, W.; Zheng, Q.; Wang, D.; Chen, Y. Fabrication of high loading V<sub>2</sub>O<sub>5</sub>/TiO<sub>2</sub> catalysts derived from metal-organic framework with excellent activity for chlorobenzene decomposition. *Appl. Surf. Sci.* **2022**, *572*, 151511. [[CrossRef](#)]
42. Ying, Q.; Liu, Y.; Li, H.; Zhang, Y.; Wu, Z. A comparative study of the dichloromethane catalytic combustion over ruthenium-based catalysts: Unveiling the roles of acid types in dissociative adsorption and by-products formation. *J. Colloid. Interface Sci.* **2022**, *605*, 537–546. [[CrossRef](#)] [[PubMed](#)]
43. Liang, W.; Zhu, Y.; Ren, S.; Li, Q.; Song, L.; Shi, X. Catalytic combustion of chlorobenzene at low temperature over Ru-Ce/TiO<sub>2</sub>: High activity and high selectivity. *Appl. Catal. A Gen.* **2021**, *623*, 118257. [[CrossRef](#)]
44. Luo, Y.; Zheng, Y.; Zuo, J.; Feng, X.; Wang, X.; Zhang, T.; Zhang, K.; Jiang, L. Insights into the high performance of Mn-Co oxides derived from metal-organic frameworks for total toluene oxidation. *J. Hazard. Mater.* **2018**, *349*, 119–127. [[CrossRef](#)] [[PubMed](#)]
45. Kan, J.; Deng, L.; Li, B.; Huang, Q.; Zhu, S.; Shen, S.; Chen, Y. Performance of co-doped Mn-Ce catalysts supported on cordierite for low concentration chlorobenzene oxidation. *Appl. Catal. A Gen.* **2017**, *530*, 21–29. [[CrossRef](#)]
46. Feng, X.; Tian, M.; He, C.; Li, L.; Shi, J.-W.; Yu, Y.; Cheng, J. Yolk-shell-like mesoporous CoCrOx with superior activity and chlorine resistance in dichloromethane destruction. *Appl. Catal. B Environ.* **2020**, *264*, 118493. [[CrossRef](#)]
47. Zhang, X.; Liu, Y.; Deng, J.; Jing, L.; Yu, X.; Han, Z.; Dai, H. Effect of transition metal oxide doping on catalytic activity of titania for the oxidation of 1,2-dichloroethane. *Catal. Today* **2021**, *375*, 623–634. [[CrossRef](#)]
48. Qiu, J.; Peng, Y.; Tang, M.; Lu, S.; Li, X.; Yan, J. Catalytic activity, selectivity, and stability of co-precipitation synthesized Mn-Ce mixed oxides for the oxidation of 1,2-dichlorobenzene. *Environ. Sci. Pollut. Res. Int.* **2021**, *28*, 65416–65427. [[CrossRef](#)]
49. Zhang, X.; Xu, Z.; Jiang, M.; Liu, Y.; Han, Z. A confinement strategy for constructing CexMn1-xO<sub>2</sub> solid solutions with oxygen vacancies confined in interwoven titania nanotubes toward catalytic ozonation of 1,2-dichloroethane. *J. Environ. Chem. Eng.* **2023**, *11*, 109299. [[CrossRef](#)]
50. Wang, Y.; Wu, S.; Wu, G.; Fang, N.; Chu, Y.; Guo, J. The abundant oxygen vacancies of the Co–Ce mixed oxides towards catalytic combustion toluene. *Microporous Mesoporous Mater.* **2022**, *343*, 112158. [[CrossRef](#)]
51. Mao, Y.; Wang, P.; Li, L.; Chen, Z.; Wang, H.; Li, Y.; Zhan, S. Unravelling the Synergy between Oxygen Vacancies and Oxygen Substitution in BiO<sub>2-x</sub> for Efficient Molecular-Oxygen Activation. *Angew. Chem. Int. Ed.* **2020**, *59*, 3685–3690. [[CrossRef](#)]
52. Liu, J.; Wang, H.; Zhang, W.; Gao, J.; Yu, Q.; Ke, J.; Wang, L. Boosting the performance of Co-doped CeO<sub>2</sub> catalyst in the catalytic oxidation of toluene by modulating oxygen vacancies. *Fuel* **2023**, *349*, 128657. [[CrossRef](#)]

**Disclaimer/Publisher’s Note:** The statements, opinions and data contained in all publications are solely those of the individual author(s) and contributor(s) and not of MDPI and/or the editor(s). MDPI and/or the editor(s) disclaim responsibility for any injury to people or property resulting from any ideas, methods, instructions or products referred to in the content.